



**Discharge voltage profile changes via physicochemical phenomena in cycled all-solid-state cells based on Li<sub>10</sub>GeP<sub>2</sub>S<sub>12</sub> and LiNbO<sub>3</sub>-coated LiCoO<sub>2</sub>**

Journal:	<i>Journal of Materials Chemistry A</i>
Manuscript ID	TA-ART-06-2021-004750.R1
Article Type:	Paper
Date Submitted by the Author:	07-Aug-2021
Complete List of Authors:	<p>Sun, Xueying; Tokyo Institute of Technology - Suzukakedai Campus, Department of Chemical Science and Engineering, School of Materials and Chemical Technology</p> <p>Yamada, Yuto; Tokyo Institute of Technology - Suzukakedai Campus, All-Solid-State Battery Unit, Institute of Innovative Research (IIR), Tokyo Institute of Technology, 4259 Nagatsuta, Midori, Yokohama 226-8502, Japan</p> <p>Hori, Satoshi; Tokyo Institute of Technology, Research Center for All-Solid-State Battery, Institute of Innovative Research (IIR)</p> <p>Li, Yuxiang; Tokyo Institute of Technology - Suzukakedai Campus, Department of Chemical Science and Engineering, School of Materials and Chemical Technology</p> <p>Suzuki, Kota; Tokyo Institute of Technology, Department of Chemical Science and Engineering, School of Materials and Chemical Technology</p> <p>Hirayama, Masaaki; Tokyo Institute of Technology, Department of Chemical Science and Engineering, School of Materials and Chemical Technology</p> <p>Kanno, Ryoji; Tokyo Institute of Technology, Research Center for All-Solid-State Battery, Institute of Innovative Research (IIR)</p>

## ARTICLE

## Discharge voltage profile changes via physicochemical phenomena in cycled all-solid-state cells based on $\text{Li}_{10}\text{GeP}_2\text{S}_{12}$ and $\text{LiNbO}_3$ -coated $\text{LiCoO}_2$

zzReceived 00th January 20xx,  
Accepted 00th January 20xx

DOI: 10.1039/x0xx00000x

Xueying Sun <sup>a</sup>, Yuto Yamada <sup>b</sup>, Satoshi Hori <sup>b</sup>, Yuxiang Li <sup>a</sup>, Kota Suzuki <sup>a</sup>, Masaaki Hirayama <sup>a</sup>, and Ryoji Kanno <sup>\*b</sup>

In the field of all-solid-state Li-ion batteries, understanding and controlling contact loss and interfacial reactions in composite electrodes over long-term cycling remains challenging. This study investigated how various physicochemical phenomena individually affect the discharge profile upon cycling for a solid-state cell with the following composition:  $\text{LiNbO}_3$ -coated  $\text{LiCoO}_2$ + $\text{Li}_{10}\text{GeP}_2\text{S}_{12}$  |  $\text{Li}_{10}\text{GeP}_2\text{S}_{12}$  | In–Li alloy. Two specially designed cells were prepared to separately characterise contact loss or interfacial chemical reactions, by means of electrochemical measurements and chemical analysis. It was found that in the discharge process, contact loss induced a certain overpotential compared to the initial value, while the chemical reaction accounted for the capacity loss caused by an additionally increased overpotential in the final stage of the discharge process. The overpotential from the undesired chemical reaction was proposed to be due to the high Li-ion transfer/migration resistance induced by sulphate formation and the decrease in the lithium content at the  $\text{LiNbO}_3/\text{Li}_{10}\text{GeP}_2\text{S}_{12}$  interface.

### Introduction

All-solid-state batteries (ASSBs) are promising energy storage devices due to their potential for enhancing the energy–power relationship<sup>1, 2</sup> and for increasing the operational temperature range;<sup>3</sup> however, ongoing issues related to capacity loss during cycling must still be addressed. Previous studies into cathode composite electrodes after cycling have established that cyclic degradation of the cathode can be separated into mechanical and chemical factors.<sup>4–6</sup> The former mainly represents the contact loss between particles, which is induced by the volume change of the cathode active material (CAM) particles during long-term cycling of the charge–discharge process.<sup>7, 8</sup> The latter includes structural changes in the CAM,<sup>9</sup> and the interfacial reaction between the CAM and the solid electrolyte (SE), which tends to produce unwanted interphases with high resistances when the SE is a sulphide.<sup>10, 11</sup> Thus, to minimise the chemical reaction taking place between the CAM and the sulphide SE, various coating materials, such as  $\text{LiNbO}_3$ ,  $\text{Li}_2\text{SiO}_3$ , and  $\text{Li}_4\text{Ti}_5\text{O}_{12}$ , have been applied as buffer layers in sulphide-based ASSBs.<sup>12–14</sup>

Although the importance of these mechanical and chemical factors has been widely acknowledged,<sup>15</sup> their respective contributions to capacity loss in the discharge profiles during charge–discharge cycling have not been fully clarified. More specifically, it is still necessary to understand how each of these factors influences the discharge voltage profile upon cycling, where an overpotential arises from a low state of discharge (SoD), and sharply increases as the SoD becomes high.<sup>10</sup>

Thus, we herein report our investigation into cells with the structure:  $\text{LiNbO}_3$ -coated  $\text{LiCoO}_2$  (LNO-coated LCO)+ $\text{Li}_{10}\text{GeP}_2\text{S}_{12}$  (LGPS) | LGPS | In–Li alloy (i.e., composite cathode | SE | anode), to understand the influences of the mechanical factors (i.e., contact loss) and the chemical factors (i.e., the interfacial reaction) on the discharge process. For this purpose, discharge profiles from the composite electrode after charge–discharge cycling are compared with those of two tailored composite electrodes. One of the two designed electrodes is prepared by re-pressing a composite after cycling with the aim of compensating particle-contact loss, while the other is prepared by heating treating at 300 °C prior to cell assembly to induce the chemical reaction and highlight its influence. Via electrochemical analysis of the two special cells, we intend to separately characterise how mechanical and chemical factors affect the discharge voltage profile changes. To obtain details of interfacial chemical reactions and relate them to discharge performance, the electrodes after 100 cycles are examined using a range of analytical techniques, including scanning transmission electron microscopy (STEM), energy-dispersive X-ray spectroscopy (EDX), and electron energy loss spectroscopy (EELS).

<sup>a</sup> Department of Chemical Science and Engineering, School of Materials and Chemical Technology, Tokyo Institute of Technology, 4259 Nagatsuta, Midori, Yokohama 226-8502, Japan

<sup>b</sup> Research Center for All-Solid-State Battery, Institute of Innovative Research (IIR), Tokyo Institute of Technology, 4259 Nagatsuta, Midori, Yokohama 226-8502, Japan

## Experimental

### Material preparation

LGPS was synthesised according to the literature.<sup>16, 17</sup> LCO (C-5H, average size: 7.96  $\mu\text{m}$ , Nippon Chemical Industrial, Japan) was coated with a layer of LNO according to the sol-gel method, or using a rolling fluidised coating machine (MP-01, Powrex, Japan),<sup>18</sup> to give a layer with a nominal thickness of 16 or 10 nm, respectively. The former LNO-coated LCO was used in the cells subjected to STEM, EDX, and EELS measurements, where a thicker coating layer enabled clearer observations. For preparation of the cathode composite, the LNO-coated LCO powder was annealed at 350 °C for 1 h under air, and then mixed with LGPS using a mill pot rotator (ANZ-10S, Nitto Kagaku, Japan) for 5 min in a weight ratio of 70:30.<sup>19</sup>

### Cell Assembly

The In–Li alloy was obtained by pressing a piece of Li foil ( $\phi$ 5 mm, thickness: 0.1 mm) into In foil ( $\phi$ 10 mm, thickness: 0.1 mm), and the resulting alloy was used as the anode. Aluminium and copper mesh were used as the cathode and anode current collectors, respectively. For the STEM, EDX, and EELS observations, cell pellets composed of CAM+LGPS | LGPS | In–Li were assembled according to the literature.<sup>20</sup> A pressure of *ca.* 80 MPa was applied to the cells during electrochemical measurements. For the tailored cells using the composites that had been repressed after the cycling test or heated prior to the cycling test, the corresponding treatment details are described in the related parts of the Results and Discussion section. For comparison purposes, cells without composites that had undergone these specific treatments are referred to as normal cells.

### Electrochemical measurements

All electrochemical tests were measured at 25 °C. The charge–discharge tests were conducted at 1.9–3.6 V using a constant current (CC) and constant voltage (CV) protocol<sup>19</sup> (TOSCAT-3100, Toyo System, Japan). During charging, a current density of 0.122 mA  $\text{cm}^{-2}$  (0.2 C rate) was applied until the voltage reached 3.6 V (CC stage). Subsequently, the voltage was maintained at a constant value (i.e., 3.6 V) until the current density had decreased to the limit of 0.02 C (CV stage). During discharge, the CC and CV rates were 1 and 0.01 C, respectively. The discharge capacity normalised using the 1<sup>st</sup> discharge capacity for the CV mode is presented in each case. The initial discharge curve of the normal cell was taken as a reference to discuss the potential differences between the discharge curves of the cycled normal cell and the tailored cells. In the discussion, this potential difference is referred to as the overpotential. Furthermore, electrochemical impedance spectroscopy (EIS) was carried out for each cell in the charged state (3.6 V vs. Li<sup>+</sup>/In–Li alloy) with an applied excitation voltage of 10 mV in a frequency range of 10<sup>6</sup> to 10<sup>-2</sup> Hz using an electrochemical measurement system (VSP-300, Biologic, France).

### X-ray photoelectron spectroscopy (XPS)

X-ray photoelectron spectroscopy (XPS) was used to observe the chemical states of the elements present in the composite cathodes. The spectra were collected using a spectrometer (1700R ESCA, ULVAC-PHI, Japan) equipped with a hemispherical analyser under ultra-high vacuum conditions using a monochromatised Al  $K\alpha$  source with a photon energy of 1486.6 keV. The composite cathodes were removed from the cells and transferred to the vacuum chamber using an airtight sample vessel. The pass energy of the analyser was 23.5 eV for the high-resolution spectra, and an energy step of 0.1 eV was employed. For the purpose of data analysis, charge compensation was employed using an ion gun, and the binding energy (BE) was corrected by calibration to the C 1s photoemission peak of adventitious hydrocarbons (C–H) at 284.8 eV. The peak locations and peak widths were obtained using the Shirley background subtraction method<sup>21</sup>, and the data were analysed using the CasaXPS software package (version 2.3.19).

### STEM, EDX, and EELS

The interface structure, elemental diffusion, and chemical states in the composite cathode of the cells after 100 charge–discharge cycles were characterised using an STEM instrument (JEM-ARM200F Dual-X, JEOL, Japan) equipped with an EDX probe (JED-2300, JEOL, Japan), and also by EELS (Enfinium ER, Gatan, USA). The high-angle annular dark-field (HAADF) STEM images were acquired using the STEM system. The elemental distribution within the interface region was mapped by EDX. The chemical states and distributions of lithium was acquired by EELS scanning with an energy resolution of <0.5 eV (full width at half maximum), and the data were treated in the equipped system (US1000XP/FT, Gatan, USA).

## Results and discussion

This section begins with describing the difference in capacity retention between the CC and CV modes to emphasise that the cyclic degradation in this type of cell is mainly due to the increased interfacial resistance. Subsequently, origins of the resistance, such as that induced by particle contact loss and interfacial chemical reaction, are investigated and their respective impacts on the discharge profile are clarified with the help of two types of tailored cells (i.e., the re-pressed cell and the cell with heating-treated cathode). First, the impact of cyclic particle contact loss is clarified by electrochemical analysis of the re-pressed cell. Then, the more significant impacts from interfacial chemical reaction are elucidated by analysing the similarity between cycled cathode and heating-treated cathode. Finally, the interfacial changes in the cycled cathode are characterised by the STEM/EDX/EELS, in order to connect individual interfacial chemical reactions and discharge profile changes.

### Comparison between the discharge capacities in the CC and CV modes

Figure 1(a) shows the 1<sup>st</sup> and the 100<sup>th</sup> discharge curves for the cells in the CC and CV modes, wherein a remarkable overpotential and

capacity loss was observed in the discharge process of the CC mode for the 100<sup>th</sup> cycle. In addition, Fig. 1(b) shows variation in the cell capacity with increasing cycle number, wherein the retention rate of the capacity for the CC (1C rate) mode was 70% at the 100<sup>th</sup> cycle, while that for the CV mode (0.02 C rate) was >95%. The capacity fading for the CC mode is in consistent with that of the results from previous similar studies.<sup>10</sup> A previous study into the mechanical factors involved in such processes proposed that particle collapse<sup>10</sup> or the irreversible phase transfer of the CAM from a layered structure to a disordered spinel or rock-salt structure would induce the formation of electrochemically inactive LCO particles.<sup>22</sup> The capacity loss induced by such inactive LCO particles should therefore take place irrespective of the discharge current rate. In contrast, the present cell exhibited a high capacity retention under a low current rate in CV mode, which was 30% higher than the capacity obtained in CC mode. This observation indicates that the LCO in the solid-state cell did not undergo significant structural collapse or irreversible phase transfer. Instead, the main reason for the decrease in capacity was considered to be a result of the increased cell resistance at the cathode side, as pointed out by an early study on EIS,<sup>10</sup> and as confirmed herein (see a later part of the discussion). This resistance increase can be attributed to chemical reactions between the LNO-coated LCO and the LGPS, and also to a reduction in the contact area between particles, as discussed in the following subsections.

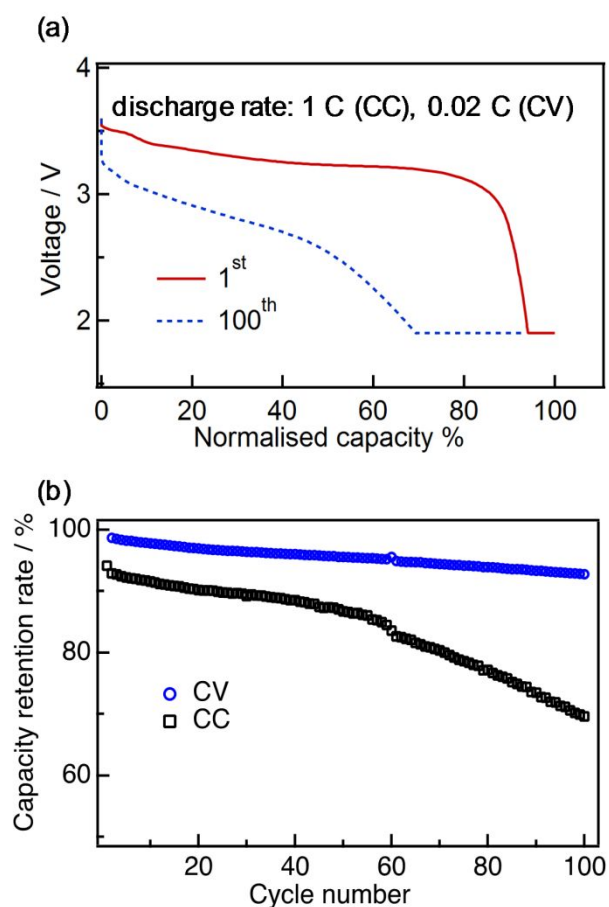


**Fig. 1** Cyclic degradation properties of the cell. (a) The discharge profiles of the 1<sup>st</sup> and 100<sup>th</sup> cycles obtained using CC (1 C) and CV (0.02 C) discharge protocols. (b) Variation in the cyclic capacity retention for the CC and CV modes upon increasing the cycle number.

#### Reduced contact area between particles in the composite cathode

The reduced particle contact area between particles in the composite cathode due to the volume change of the CAM particles during the charge–discharge process was indicated by previous studies.<sup>23</sup> Our study confirmed the uneven contact loss between particles in the composite cathode of cells by *in situ* FE-SEM observations. (see Fig. S1 in the Supporting Information for detailed images) To clarify the influence of this mechanical contact decrease on discharge profile, the cathode composite re-pressed after charge–discharge cycling was investigated.

Figure 2(a) outlines the cell re-pressing process employed to compensate for the decreased contact area. As indicated, after 50 charge–discharge cycles at a rate of 1 C, the composite cathode was removed from the cell, and was re-pressed under a pressure of 178 MPa for 10 s. Subsequently, the re-pressed cathode was combined with the original anode pellet that had undergone 50 charge–discharge cycles. Finally, the re-pressed cell was subjected to subsequent charge–discharge testing; if the process of re-pressing can fully compensate for the decreased contacts between particles, the induced capacity degradation should be ideally compensated.

Figure 2(b) shows the discharge curves obtained at the 1<sup>st</sup> and 50<sup>th</sup> cycles carried out prior to re-pressing, in addition to that obtained after re-pressing. As indicated, the discharge capacity reached 115 mAh g<sup>-1</sup> in the 1<sup>st</sup> cycle, and decreased to 94 mAh g<sup>-1</sup> in the 50<sup>th</sup> cycle. After re-pressing of the cell cathode, the capacity recovered to a small extent. Meanwhile, the discharge voltage difference compared to the 1<sup>st</sup> cycle (referred to as overpotential in this study) was obviously reduced especially at the initial SoD. More specifically, the initial voltage difference between the 1<sup>st</sup> cycle (black solid curve in Fig. 2(b)) and the 50<sup>th</sup> cycle (black dotted curve) was 0.32 V, while that between the 1<sup>st</sup> cycle and re-pressed (red dotted curve) was 0.14 V. With the assumption that the contact decrease was significantly compensated after re-pressing, the obtained results suggested that the contact decrease between particles caused a constant overpotential starting from the initial SoD. Therefore, the uncompensated overpotential and capacity loss should be attributed to the chemical reaction taking place in the cathode, as well as interphase formation between the SE and the anode side.<sup>24</sup> Little discharge capacity compensated after the re-press process indicates that the chemical reaction at cathode as well as anode interfaces had more impact on the capacity loss than the particle–particle contact decrease. Figure 2(c) shows the Nyquist plots from the EIS measurements carried out on the cell after 50 cycles (top) and after re-pressing (bottom). The resistances were analysed by a typical equivalent circuit model for the solid-state cell,<sup>10</sup> as outlined in Fig. S2, and the fitting data are given in Table S1 of the Supporting Information. From the obtained results, it is apparent that the resistances at the cathode side, which are

included in the two semicircles at the high-frequency side, became smaller after re-pressing; the contributions from R1 and R2 decreased by  $458 \Omega$ , giving a value approximately half that obtained before re-pressing. This variation in resistance coincided well with the discharge profiles shown in Fig. 2(b), where the overpotential at the beginning of discharge reduced by approximately half following re-pressing (i.e., from 0.32 to 0.14 V).

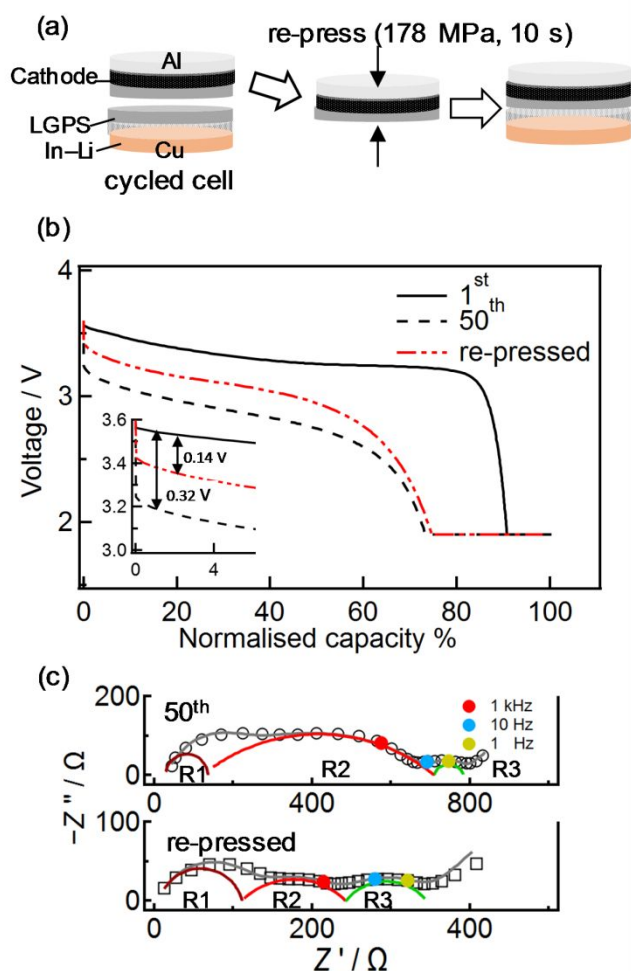


**Fig. 2** Influence of the reduced mechanical contact on the electrochemical properties. (a) The re-pressing process. (b) Discharge profiles obtained with a rate of 1 C for the 1<sup>st</sup> and 50<sup>th</sup> cycles before re-pressing, and that of the 1<sup>st</sup> cycle after re-pressing. The inserted panel indicates the overpotential change at low SoD stage from 0.32 V (at the 50<sup>th</sup> cycle) to 0.14 V (after re-pressed). (c) Nyquist plots of the cell after 50 cycles (top), and of the cell after re-pressing (bottom). The R | CPE components are denoted with differently coloured circles according to their specific frequencies.

#### Heating of the electrode composite to enhance the chemical reaction at the cathode side

The results on re-pressed cathode implied that rather than contact loss, chemical reactions in cathode composite had more significant impacts on cycle-induced capacity decrease. To rapidly enhance the chemical reaction at the LCO/LNO/LGPS interface for observation and characterisation purposes, the composite cathode pellet was

heated at 300 °C under a  $< 10^{-3}$  Pa vacuum for 10 h, as outlined in Fig. 3(a). The electrochemical properties of the cell prepared using the heated cathode (i.e., the “heated cell”) were then investigated. Previous studies have reported that the interfacial reaction between LCO/LGPS will induce changes in the S 2p XPS profile.<sup>10, 25</sup> Thus, the S 2p signal was used as an indicator for the chemical reaction at the cathode side. Figure 3(b) shows the spectra collected from the cathode of the normal cell before cycling (Non-cycled) and after 100 charge–discharge cycles (Cycled), in addition to that of the heated cell (Heated) after 1 charge–discharge cycle. The spectrum of the non-cycled sample exhibited a single peak, i.e., the S<sup>2-</sup> peak (peak-A), which was attributed to the original LGPS crystal. In contrast, the spectrum of the cycled sample also showed peaks corresponding to oxidised sulphur species, including –S–S– (peak-B, ~164 eV)<sup>10</sup> and SO<sub>x</sub> (peak-C, sulphate with a BE at 168–171 eV).<sup>26</sup> The spectrum of the heated sample was similar to that of the cycled sample, suggesting that the two samples possess similar interfacial chemical states. The spectra of the other elements present in the cathode also show similarities between the cycled and heated samples (see Fig. S3 in the Supporting Information). Based on these XPS results, we considered that the type and degree of the chemical reaction taking place in the composite electrode were similar for the cycled and heated samples.

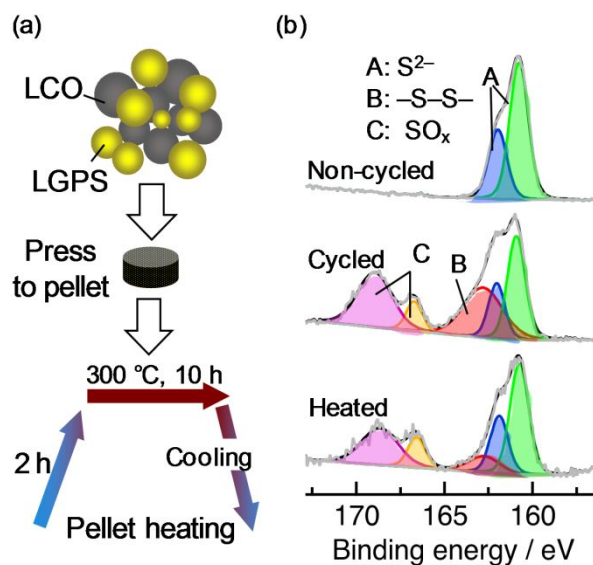


**Fig. 3** Enhanced chemical degradation in the cathode upon heat treatment. (a) Outline of the heat treatment process used to enhance the chemical reaction in the cathode composite. (b) The XPS spectra for the S 2p edge collected from the cathodes of the normal cell before cycling (Non-cycled) and after 100 cycles (Cycled), and from the cathode of the heated cell after 1 cycle (Heated).

The heated cathode, in which the influence of the decreased particle contact was excluded, was then investigated to clarify the influence of the chemical reaction on the discharge capacity during long-term cycling. Figure 4(a) shows the Nyquist plots of the heated

cell, as well as those of the normal cell after the 1<sup>st</sup> and 100<sup>th</sup> cycles; the fitting parameters are listed in Table S1 of the Supporting Information. These plots are consistent with each cell condition. More specifically, in the heated cell, the resistance components denoted as R1 and R2 are larger than those of the normal cell after 1 cycle. This increase is due to the heat-induced resistance at the cathode side, since a non-cycled In–Li anode was used in the heated cell, and thus the influence of the interfacial reaction between the anode and the SE side was negligible. On the other hand, the total resistance of the heated cell was smaller than that of the cycled cell. The large margin of resistance in the cycled cell can be reasonably ascribed to the resistive layer at the anode side and the decreased contact area at the cathode. The total resistances of the cycled cell and the heated cell increased by 726 and 142  $\Omega$  (5:1 ratio), respectively, compared with that of the normal cell after the 1<sup>st</sup> cycle (105  $\Omega$ ). With regard to the respective discharge profile for each cell, the resistance increase will cause at least one kind of overpotential, such as that appearing from the beginning of the discharge process, which is less dependent on the SoD.

Figure 4(b) compares the discharge curves of the normal and heated cells. Compared with the 1<sup>st</sup> cycle of the normal cell, a constant overpotential of  $\sim 0.1$  V was observed in the heated cell in a low SoD stage, which corresponded to the normalised capacity range between 0 and 40%. The observed overpotential is  $\sim 1/5$  that of the cycled cell, which is consistent with results of the EIS measurements. This consistence is in line with the indication from XPS results that the chemical reaction taking place at the cathode side in the cycled cell was well simulated in the heated cathode. The inference is supported by considering the degree of capacity loss; the 1<sup>st</sup> discharge capacity for the heated cell suffered a 35% decrease compared with that of the normal cell, and this value is similar to the capacity loss for the normal cell at the 100<sup>th</sup> cycle.

To obtain further insight, the discharge profiles of the cycled cell and the cell containing the heated cathode were compared after equalising their overpotentials at the initial SoD with a normalised capacity of 0%. This was achieved through equalisation by vertically shifting the cycled discharge profiles in an upwards direction by 0.4 V (see Fig. 4(b)); this numerical operation corresponds to eliminating the overpotentials induced by a resistance increase through interphase formation at the anode side and decreased particle contact at the cathode side. As a result, the two profiles reasonably overlapped; the overpotential was constant at a low SoD with a normalised capacity up to 40%, whereas it sharply increased at a higher SoD. This profile overlap further confirms that the overpotentials from the cathode-side chemical reactions are similar for the two degraded cells. From the above analysis, two conclusions were drawn regarding the overpotentials in the cycled cells: 1) The initial type of overpotential remains constant at a lower SoD, and is caused by the chemical reaction at the anode side, a decrease in the particle contact area in the cathode, and the chemical reaction at the cathode side; and 2) the additional overpotential observed at a higher SoD, which sharply increases with increasing SoD, can be attributed to the chemical reaction at the cathode side.

As discussed in terms of the EIS measurements for the cycled cell, the overpotentials at the lower SoD side can be explained by considering the resistances induced by the respective physical/chemical phenomenon. In terms of the sharp overpotential increase at a higher SoD, which is induced by unwanted reactions at the cathode side, the mechanism is not straightforward. Such complexity arises from the fact that the resistance for diffusion relating to the CAM increases depending on the SoD. Namely, the Li-ion diffusion from the bulk to the surface of the CAM particle usually will become slow along with the SoD increasing. Especially when the SoD is near 100%, the sluggish in diffusion is much significant.<sup>27</sup>

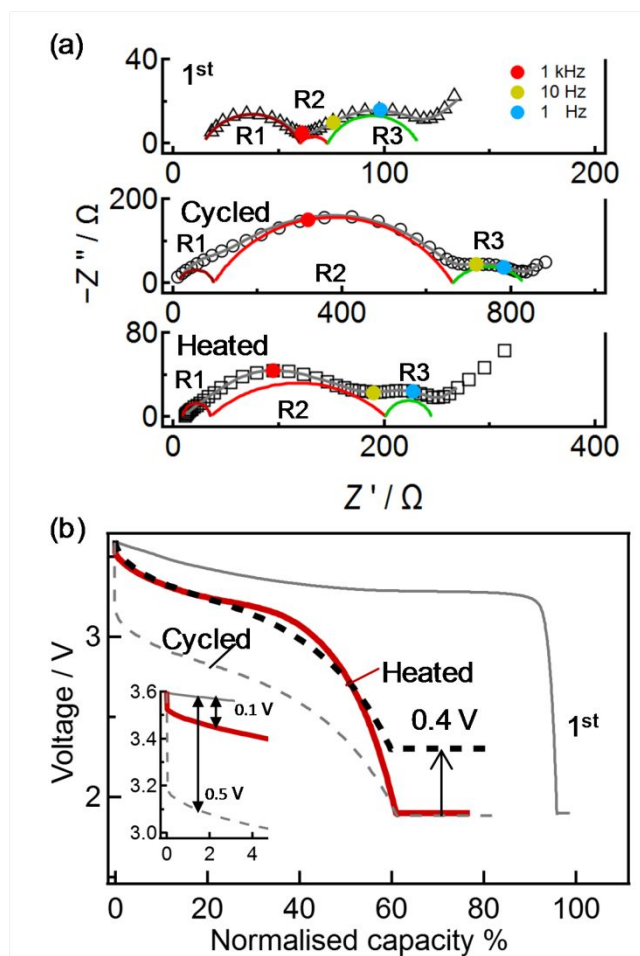


**Fig. 4** Influence of chemical degradation on the electrochemical performance of the cells. (a) Nyquist plots of the normal cell after the 1<sup>st</sup> and 100<sup>th</sup> cycles, and for the heated cell after the 1<sup>st</sup> cycle (top to bottom). The R | CPE components are denoted by differently coloured semicircles according to their specific frequencies. (b) Comparison of the charge–discharge performances of the normal (1<sup>st</sup> and 100<sup>th</sup> cycles) and the heated (1<sup>st</sup> cycle) cells. The inserted panel indicates at low SoD stage the overpotential of the heated cell is  $\sim 1/5$  smaller than that of the cycled cell.

#### Characterisation of the chemical changes taking place at the cathode interface

The chemical phenomena in the cycled cathode side were characterised to determine their relationship with the resistance increase in the cathode at a higher SoD. The bulk LCO and the LCO/LNO interface region after cycles were investigated via the high-resolution TEM and EELS analyses (see Figs. S4-S6 in the Supporting Information). We confirmed the stability of bulk LCO after cycles, which is consistent with the high retention-rate value in discharge capacity at CV mode (see Fig. 1), as well as the reported studies<sup>28–30</sup>. Moreover, we found that the LCO/LNO interface region also kept stable after 100 cycles.

For the LCO/LNO/LGPS interfaces in the composite cathode, elemental diffusion was characterised by STEM/EDX for the cells before cycling (Non-cycled) and after 100 charge–discharge cycles (Cycled). Figure 5(a) shows the EDX mapping images of the interface region, where the LNO/LCO boundary was clearly observed, indicating that no elemental diffusion occurred across this interface. Figure 5(b) shows the EDX mapping images for the cathode interface in the cycled cell, where once again, a clear boundary between the LCO and LNO layers was observed, while the niobium and sulphur areas became overlapped. This observation indicates that the LNO layer contained sulphur but not cobalt. These results therefore confirmed that the chemical reaction occurred within the LCO/LNO/LGPS interface region after charge–discharge cycling. In particular, analysis by STEM-EDX indicated that sulphur diffused into the LNO layer during cycling, thereby confirming that the chemical reaction involved LNO/LGPS side.

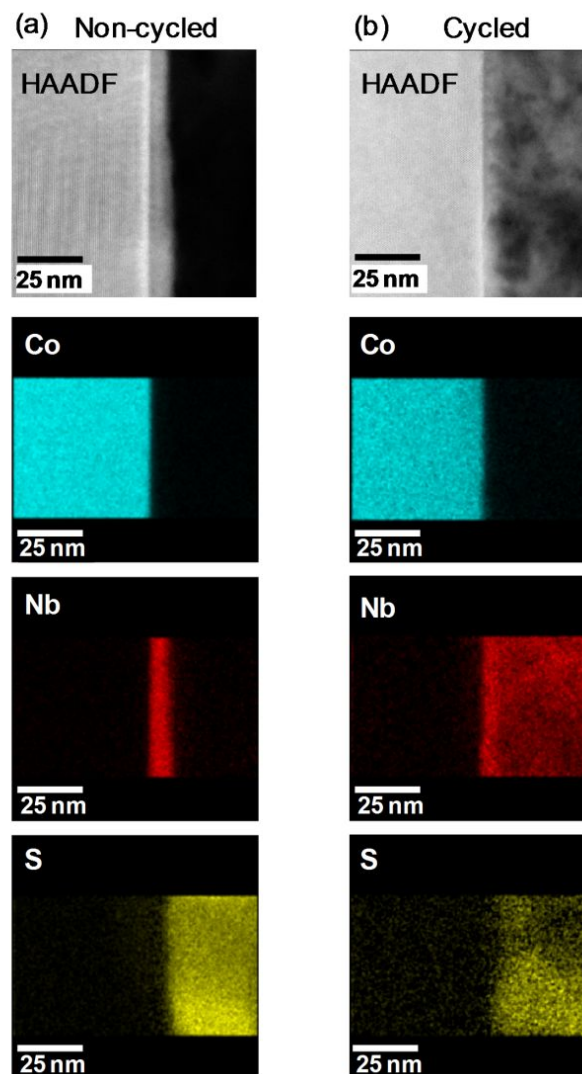


**Fig. 5** STEM/EDX characterisation of elemental diffusion in the composite cathode. HAADF image of the EDX mapping region, and mapping of Co, Nb, and S for (a) the cell before cycling (Non-cycled), and (b) the cell after 100 charge–discharge cycles (Cycled).

As the formation of sulphate in the composite cathode has been confirmed by XPS, it was proposed that the lithium content will correspondingly suffer a decrease in the LNO/LGPS interface.<sup>10, 31, 32</sup> The HAADF images with EELS-scanning shown in Fig. 6 confirmed the decrease of lithium content in the LNO layer.

Figure 6 shows the EELS spectra obtained close to the Li\_K edge, which were measured along the area of the HAADF image for the non-cycled and cycled cells. The HAADF image shown in Fig. 6(a) includes the LCO/LNO/LGPS interfaces; the corresponding spectra coloured in black, red, green, brown and blue (from bottom to top) were collected from the LCO bulk, LCO/LNO interface, LNO layer, LNO/LGPS interface and the LGPS, respectively. The investigated area represented in Fig. 6(b) only includes the LCO/LNO layers.

Four characteristic peaks were found in the EELS spectra close to the Li\_K edge for the non-cycled cell (Fig. 6(a)). More specifically, peak-A (58–61 eV) was ascribed to the Li\_K edge,<sup>33</sup> while peak-B

(62–65 eV) was considered to be the scattering main peak of the Li\_K edge,<sup>34</sup> which overlapped with the Co\_M<sub>2,3</sub> edge<sup>35</sup> in the LCO layer. As indicated, peak-A and peak-B were observed over the whole LCO layer (spectra coloured in black), and in the LNO layer (spectra coloured in green). The range of the LNO layer was identified using a peak-pair from niobium species,<sup>36</sup> which was observed at ~40 and 45 eV, and denoted as peak-C and peak-D, respectively. As can be seen, peak-A shifted to the lower energy loss side, indicating a change in the chemical environment around the Li atoms across the LNO/LGPS interface (brown) and LGPS (blue); this was attributed to a change from Li–O to Li–S bonding. As expected, the EELS observations made close to Li\_K for the cycled cell (Fig. 6(b)) differed from those of the non-cycled cell.

More specifically, in the cycled cell, peak-A and peak-B were clearly observed in the LCO layer (black spectral lines), but these peaks gradually disappeared upon approaching the LCO/LNO interface (red spectral line) and in the LNO layer (green spectral lines). The Li content change inside LNO layer after charge–discharge cycling was clearly detected by comparing relative intensities for peak-A from the respective LNO layer of non-cycled or cycled cell. The intensity ratio of peak-A to -D is ~0.4 for the former, while that for the latter is as small as < 0.1, indicating a significant decrease in the lithium content of the LNO layer after the cycle test.

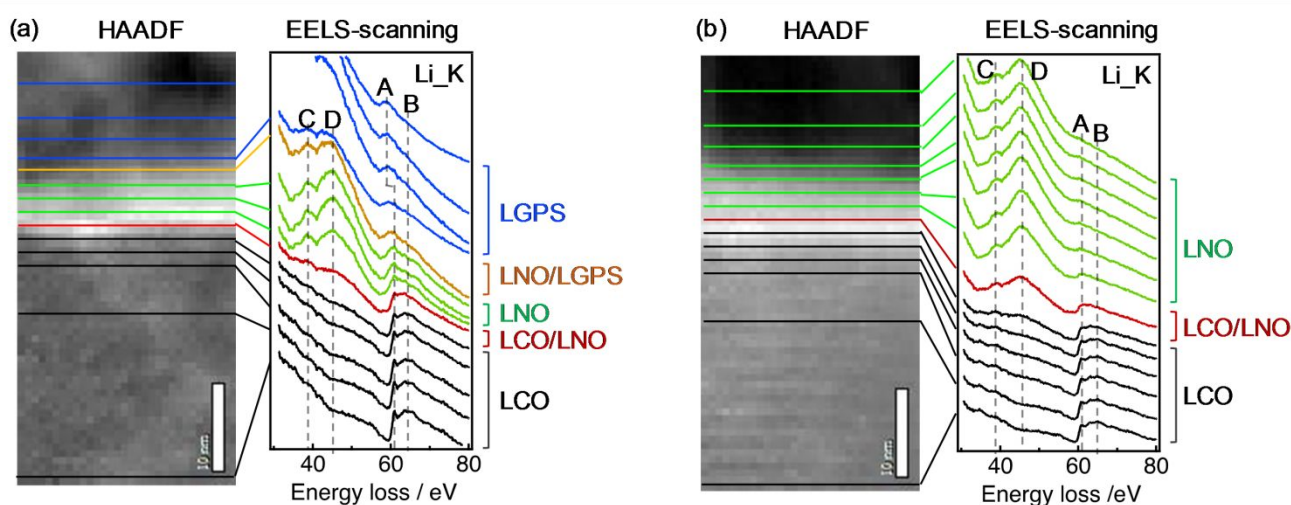


Fig. 6 HAADF images and the corresponding EELS line scans near Li\_K edges across the interface for (a) the non-cycled cell, and (b) the cycled cell.

### Influences of chemical changes on voltage profile

The above chemical characterisation therefore confirmed that the chemical reaction mainly occurred at the LNO/LGPS interface area, as represented by the diffusion of sulphur from the LGPS to the LNO layer and a decrease in the Li content at the interface region. In addition to the reported formation of interphases such as elemental sulphur, metal sulphates, germanium oxides and metaphosphates,<sup>10, 37</sup> this cycle-induced reduction in the lithium content through the cathode-side reaction, therefore is proposed as the main cause of changes in the discharge profile of the cell. More specifically, the cycled LNO coating layer containing undesired interphases and a reduced amount of lithium slows down Li-ion transfer across the interfacial layer into the bulk LCO. In extreme cases, this could render the LCO surface electrochemically inactive, with the Li-ion conduction pathways being completely cut off. Since the present cycled cell showed a higher capacity retention when discharged at a rate of 0.01 C (CV mode), it was speculated that the cycle-induced deactivation of LNO-LCO only partially occurred on the surface. During discharge at a high current rate (i.e., 1 C), the flow of lithium ions onto surface of the electrochemically active LCO layer results in an area with locally high SoD of up to 100% in the middle of a single discharge step. This inhomogeneous reaction

would inevitably induce a sharp increase in overpotential in the discharge profile as the SoD becomes higher, therefore accounting for an almost complete capacity loss. The above mechanism, which connects the degree of Li content reduction around the LCO to the discharge profile after cycling, implies that the search for Li-rich coating layers should be considered for next-generation ASSBs with higher cycle performances. For screening and selecting a cyclic and stable coating-layer/SE interface, the present approach to simulate cycle-induced chemical reactions by post heating of the cathode composite will be helpful.

### Conclusions

In the context of an all-solid-state battery (ASSB, composition: LiNbO<sub>3</sub>-coated LiCO<sub>2</sub>+Li<sub>10</sub>GeP<sub>2</sub>S<sub>12</sub> | Li<sub>10</sub>GeP<sub>2</sub>S<sub>12</sub> | In–Li alloy), we herein investigated the influences of a reduced mechanical contact and chemical reactions at the cathode side on the cyclic changes taking place in the battery discharge profile. Both of these physicochemical phenomena caused a constant overpotential from the initial state of discharge (SoD), although the latter was the main reason for the capacity loss induced by a sharp increase in the overpotential at a high SoD. Detailed chemical analysis indicated

the formation of sulphate and a remarkable decrease in the Li content in the  $\text{LiNbO}_3/\text{Li}_{10}\text{GeP}_2\text{S}_{12}$  interface region, which were presumably responsible for the increased Li-ion resistance during discharge. Thus, the present work proposed that the Li concentration in the coating layer of the cathode active material is a key parameter to improve capacity retention in ASSBs after long-term cycling.

## Supporting Information

Supporting Information is available online at xxxx.

## Author Contributions

The manuscript was written through contributions of all authors. All authors discussed the results, contributed to the manuscript writing, and approved its final version.

## Conflicts of interest

There are no conflicts to declare.

## Acknowledgements

This research was partly supported by the Program on Open Innovation Platform with Enterprises, Research Institute and Academia (OPERA) Program [JPMJOP1862] from the Japan Science and Technology Agency (JST). R.K. acknowledges support from the Grant-in-Aid for Scientific Research [S, no. 17H06145]. M.H. and K.S. acknowledge the support from a Grant-in-Aid for Scientific Research on Innovative Areas [19H05785]. X.S. thanks the financial supports from the Japan student services organisation (JASSO).

## References

1. S. Randau, D. A. Weber, O. Kötz, R. Koerver, P. Braun, A. Weber, E. Ivers-Tiffée, T. Adermann, J. Kulisch and W. G. Zeier, *Nature Energy*, 2020, **5**, 259–270.
2. Y.-G. Lee, S. Fujiki, C. Jung, N. Suzuki, N. Yashiro, R. Omoda, D.-S. Ko, T. Shiratsuchi, T. Sugimoto and S. Ryu, *Nature Energy*, 2020, **5**, 299–308.
3. Y. Kato, S. Hori, T. Saito, K. Suzuki, M. Hirayama, A. Mitsui, M. Yonemura, H. Iba and R. Kanno, *Nature Energy*, 2016, **1**, 1–7.
4. N. Riphaut, B. Stiaszny, H. Beyer, S. Indris, H. A. Gasteiger and S. J. Sedlmaier, *Journal of The Electrochemical Society*, 2019, **166**, A975.
5. J. A. Lewis, J. Tippens, F. J. Q. Cortes and M. T. McDowell, *Trends in Chemistry*, 2019, **1**, 845–857.
6. J. Ma, B. Chen, L. Wang and G. Cui, *Journal of Power Sources*, 2018, **392**, 94–115.
7. M. Nakayama, S. Wada, S. Kuroki and M. Nogami, *Energy & Environmental Science*, 2010, **3**, 1995–2002.
8. R. Koerver, W. Zhang, L. de Biasi, S. Schweidler, A. O. Kondrakov, S. Kolling, T. Brezesinski, P. Hartmann, W. G. Zeier and J. Janek, *Energy & Environmental Science*, 2018, **11**, 2142–2158.
9. X. Li, Z. Ren, M. Norouzi Banis, S. Deng, Y. Zhao, Q. Sun, C. Wang, X. Yang, W. Li and J. Liang, *ACS Energy Letters*, 2019, **4**, 2480–2488.
10. W. Zhang, F. H. Richter, S. P. Culver, T. Leichtweiss, J. G. Lozano, C. Dietrich, P. G. Bruce, W. G. Zeier and J. r. Janek, *ACS applied materials & interfaces*, 2018, **10**, 22226–22236.
11. S.-K. Jung, H. Gwon, S.-S. Lee, H. Kim, J. C. Lee, J. G. Chung, S. Y. Park, Y. Aihara and D. Im, *Journal of Materials Chemistry A*, 2019, **7**, 22967–22976.
12. K. Takada, N. Ohta, L. Zhang, K. Fukuda, I. Sakaguchi, R. Ma, M. Osada and T. Sasaki, *Solid State Ionics*, 2008, **179**, 1333–1337.
13. A. Sakuda, A. Hayashi and M. Tatsumisago, *Chemistry of Materials*, 2010, **22**, 949–956.
14. N. Ohta, K. Takada, I. Sakaguchi, L. Zhang, R. Ma, K. Fukuda, M. Osada and T. Sasaki, *Electrochemistry communications*, 2007, **9**, 1486–1490.
15. O. Sheng, C. Jin, X. Ding, T. Liu, Y. Wan, Y. Liu, J. Nai, Y. Wang, C. Liu and X. Tao, *Advanced Functional Materials*, 2021, 2100891.
16. N. Kamaya, K. Homma, Y. Yamakawa, M. Hirayama, R. Kanno, M. Yonemura, T. Kamiyama, Y. Kato, S. Hama and K. Kawamoto, *Nature materials*, 2011, **10**, 682–686.
17. D. Hayashi, K. Suzuki, S. Hori, Y. Yamada, M. Hirayama and R. Kanno, *Journal of Power Sources*, 2020, **473**, 228524.
18. N. Ohta, K. Takada, L. Zhang, R. Ma, M. Osada and T. Sasaki, *Advanced Materials*, 2006, **18**, 2226–2229.
19. W. J. Li, M. Hirayama, K. Suzuki and R. Kanno, *Solid State Ionics*, 2016, **285**, 136–142.
20. X. Sun, S. Hori, Y. Li, Y. Yamada, K. Suzuki, M. Hirayama and R. Kanno, *Journal of Materials Chemistry A*, 2021, **9**, 4117–4125.
21. D. A. Shirley, *Physical Review B*, 1972, **5**, 4709–4714.
22. W. M. Seong, K. Yoon, M. H. Lee, S.-K. Jung and K. Kang, *Nano letters*, 2018, **19**, 29–37.
23. T. Shi, Y.-Q. Zhang, Q. Tu, Y. Wang, M. Scott and G. Ceder, *Journal of Materials Chemistry A*, 2020, **8**, 17399–17404.
24. R. Kanno, M. Murayama, T. Inada, T. Kobayashi, K. Sakamoto, N. Sonoyama, A. Yamada and S. Kondo, *Electrochemical and Solid State Letters*, 2004, **7**, A455.
25. W. Zhang, D. A. Weber, H. Weigand, T. Arlt, I. Manke, D. Schröder, R. Koerver, T. Leichtweiss, P. Hartmann and W. G. Zeier, *ACS applied materials & interfaces*, 2017, **9**, 17835–17845.
26. J. Chastain, *Handbook of X-ray Photoelectron Spectroscopy*, eds, 1992.
27. Y.-M. Choi, S.-I. Pyun, J.-S. Bae and S.-I. Moon, *Journal of power sources*, 1995, **56**, 25–30.
28. Y. Lyu, X. Wu, K. Wang, Z. Feng, T. Cheng, Y. Liu, M. Wang, R. Chen, L. Xu, J. Zhou, Y. Lu and B. Guo, *Advanced Energy Materials*, 2021, **11**, 2000982.
29. K. Ozawa, *Solid State Ionics*, 1994, **69**, 212–221.
30. K. Mizushima, P. Jones, P. Wiseman and J. B. Goodenough, *Materials Research Bulletin*, 1980, **15**, 783–789.
31. F. Han, Y. Zhu, X. He, Y. Mo and C. Wang, *Advanced Energy Materials*, 2016, **6**, 1501590.
32. Y. Zhu, X. He and Y. Mo, *ACS Applied Materials & Interfaces*, 2015, **7**, 23685–23693.
33. J. Kikkawa, S. Terada, A. Gunji, T. Nagai, K. Kurashima and K. Kimoto, *The Journal of Physical Chemistry C*, 2015, **119**, 15823–15830.
34. H. O. Moltaji, J. P. Buban and N. D. Browning, *Journal of synchrotron radiation*, 1999, **6**, 326–328.
35. J. Graetz, C. Ahn, R. Yazami and B. Fultz, *The Journal of Physical Chemistry B*, 2003, **107**, 2887–2891.

## Journal Name

## ARTICLE

36. R. Sachan, O. Pakarinen, P. Liu, M. Patel, M. Chisholm, Y. Zhang, X. Wang and W. Weber, *Journal of Applied Physics*, 2015, **117**, 135902.
37. T. K. Schwietert, V. A. Arszewska, C. Wang, C. Yu, A. Vasileiadis, N. J. de Klerk, J. Hageman, T. Hupfer, I. Kerkamm and Y. Xu, *Nature materials*, 2020, **19**, 428–435.